J. Plasma Phys. (2022), *vol*. 88, 905880607
Published by Cambridge University Press

doi:10.1017/S0022377822000770

Power-transfer and fixed-point analysis of sawtooth simulations of a current-carrying stellarator

O.E. López [1],†, **E.C. Howell** [2], **J.D. Hanson** [1] **and D.A. Maurer** [1]

[1]Physics Department, Auburn University, Auburn, AL 36849, USA

[2]Tech-X Corporation, 5621 Arapahoe Ave Suite A, Boulder, CO 80303, USA

(Received 3 May 2022; revised 11 August 2022; accepted 15 August 2022)

Power-transfer and fixed-point analysis of previous NIMROD simulations (Roberds *et al.*, *Phys. Plasmas*, vol. 23, issue 9, 2016, 092513) improved the understanding of the effect of 3D (non-axisymmetric equilibrium) magnetic fields on sawtooth oscillations in the Compact Toroidal Hybrid (CTH) experiment. Computing the locations of order-1 fixed points, their Greene's residues, and local values for the rotational transform results in a description of CTH sawteeth consistent with Kadomtsev's model. A power-transfer analysis quantifies the distribution of energy among toroidal Fourier modes and their nonlinear interactions. The Lorentz power transfer drives sawtooth growth, and it is unambiguously interpreted as the flow of energy from toroidal mode n' to mode n, catalysed by $\boldsymbol{B}_{n-n'}$. It has been reported previously that the CTH sawtooth frequency increases with the 3D field strength. This is attributed to an increased growth rate of the internal kink that drives sawtooth oscillations. Here, 3D fields remove energy from the kink, eliminating the possibility that these fields are an additional energy source that drives growth. Instead, 3D fields catalyse energy transfer from large-to-small scales, where magnetic reconnection is stronger. It is proposed that this energy transfer increases the reconnection rate at small scales, which is consistent with the increased growth rate observed at higher 3D field strengths.

Key words: fusion plasma, plasma instabilities, plasma simulation

1. Introduction

The standard signature for sawtooth oscillations in a toroidal confinement device is a gradual temperature increase in the core followed by a fast crash. First reported in the ST tokamak (von Goeler, Stodiek & Sauthoff 1974), they have also been observed in stellarators (Carreras *et al.* 1998; Takagi *et al.* 2004; Varela, Watanabe & Ohdachi 2012). During the crash, there is heat redistribution and temperature flattening in the core. On tokamaks, sawteeth both degrade confinement (through enhanced transport) and

† Present address: Oak Ridge National Laboratory, Oak Ridge, TN 37831, USA. Email address for correspondence: lopezortizoe@ornl.gov

seed neoclassical tearing modes (Sauter *et al.* 1997; La Haye 2006). On the stellarator side, W7-X has observed sawtooth and sawtooth-like crashes in discharges with a strong electron cyclotron current drive (ECCD) (Zanini *et al.* 2020; Aleynikova *et al.* 2021). ECCD is used in W7-X as one strategy to balance the bootstrap current and obtain a low-shear configuration with a set of magnetic islands at the plasma edge that function as a divertor. ECCD application may locally modify the rotational transform (the ratio of poloidal over toroidal turns along a magnetic field line) profile and render the plasma susceptible to magnetohydrodynamic (MHD) instabilities. ECCD-induced sawtooth crashes affect the strike lines' position on divertor plates, and their understanding is vital to avoid component damage.

The Kadomtsev (1975) model is a standard description of sawteeth in tokamaks. In Kadomtsev's theory, a tokamak with an on-axis safety factor (q_0) below unity leads to an $n = m = 1$ internal kink mode, whose evolution causes the flattening of the central temperature and current density until $q_0 > 1$. After that, a temperature-dependent Spitzer resistivity ensures that current accumulates in the core until the on-axis safety factor drops below unity again, and the process repeats.

The Compact Toroidal Hybrid (CTH) experiment (Hartwell *et al.* 2017) is a current-carrying five-field-period ($N_{fp} = 5$) stellarator in which a variable external rotational transform enables the study of the effect of 3D magnetic fields on MHD stability. In CTH, the rotational transform (ι) is due to the magnetic field generated both by plasma current and external coil current. The plasma current is driven inductively, its rotational transform contribution is denoted by ι_{plasma}. The vacuum or external transform, ι_{ext}, can be independently controlled by currents in the helical and toroidal field coils. At the plasma edge, the value of the external transform can be set to be in the $0.02 < \iota_{\text{ext}} < 0.3$ range. CTH power supplies are inadequate to operate as a tokamak, i.e. with $\iota_{\text{ext}} = 0$. Numerically, it is possible to consider hypothetical configurations with $0 \leq \iota_{\text{ext}} \leq 0.02$. The rotational transform is given by the sum $\iota = \iota_{\text{plasma}} + \iota_{\text{ext}}$, and the safety factor is the inverse of the rotational transform ($q = 1/\iota$).

Experimental (Herfindal *et al.* 2019) and computational (Roberds *et al.* 2016) studies have evaluated the effect of external rotational transform on the sawtooth instability in CTH's stellarator scenarios (i.e. scenarios with non-zero ι_{ext}). Experiments show a reduction in the sawtooth amplitude and an increase in the sawtooth period as ι_{ext} is increased (Herfindal *et al.* 2019). The latter observation is computationally reproduced in Roberds *et al.* (2016). This work revisits 3D nonlinear NIMROD simulations of sawtooth oscillations in CTH (Roberds *et al.* 2016). We analyse these simulations with tools based on the dynamics of fixed points and the energy transfer between toroidal Fourier modes. We conclude that the fixed-point dynamics during sawtooth oscillations in tokamak and stellarator scenarios are similar. However, the stellarator fields modulate the energy transfer between Fourier modes in the stellarator configuration.

A new search algorithm that locates fixed points and calculates their associated Greene's residues in NIMROD improves the description of sawtooth cycles in CTH. Fixed points result from the intersection of a closed magnetic field line with a Poincaré cross-section. An important quantity characterising a fixed point is the Greene's residue (Greene 1968, 1979). The Greene's residue of a thin magnetic island monotonically increases with its width; the residue has been employed as a proxy for the degree of stochasticity of stellarator vacuum magnetic fields (Hanson & Cary 1984; Cary & Hanson 1986). In this work, the determination of fixed points, Greene's residues and local values for the rotational transform result in a description of sawtooth oscillations in CTH consistent with Kadomtsev's model. The present analysis may be considered a generalisation of the

https://doi.org/10.1017/S0022377822000770 Published online by Cambridge University Press

fixed-point tokamak sawtooth picture of Smiet, Kramer & Hudson (2019) to the stellarator case.

This article addresses the observed increased sawtooth frequency with 3D shaping (Herfindal *et al.* 2019). A power-transfer analysis is utilised to investigate how energy is deposited into the sawtooth instability and redistributed within the instability. This analysis determines that stellarator fields have a two-fold effect on the sawtooth instability growth. On the one hand, stellarator fields damp that sawtooth instability linear growth, implying a stabilising effect. On the other hand, stellarator fields catalyse energy transfer from large-to-small scales. It is hypothesised that this transfer of energy to small scales effectively enhances the reconnection rate, which would increase the growth rate and the sawtooth frequency.

The power-transfer diagnostic was introduced by Ho & Craddock (1991) during the exploration of the conversion of poloidal magnetic field into toroidal magnetic field (the dynamo effect) in a reversed-field pinch (RFP). It is a diagnostic tool that focuses on the dynamics of specific Fourier modes. Their framework expresses the time rate of change of the Fourier mode energy as a superposition of quasilinear, nonlinear and dissipative power-transfer terms. This analysis allowed them to 'piece together a picture of the flow of power through Fourier space' and has become a standard diagnostic tool (Sovinec 1995; Choi *et al.* 2006; Reynolds, Sovinec & Prager 2008; Futch *et al.* 2018; Howell *et al.* 2022). This article adapts the power-transfer analysis to a 3D equilibrium. Here, it is recognised that the nonlinear Lorentz power transfer obeys a specific energy conservation relation, allowing unequivocal characterisation of energy transfer between toroidal Fourier modes, including those that characterise a sawtooth oscillation in a 3D equilibrium.

The rest of the paper is organised as follows. Section 2 summarises previous work on sawtooth oscillations in CTH. Section 3 introduces the power-transfer analysis tool in the context of a 3D equilibrium, and shows that the Lorentz power-transfer coefficient is unambiguously interpretable as transfer of energy between two toroidal Fourier modes. Section 4 discusses the dynamics of fixed points during sawtooth oscillations. Section 5 considers the energy transfer between Fourier modes. A final discussion is provided in § 6.

2. Sawtooth oscillations in CTH

This work reconsiders CTH sawtooth NIMROD simulations with increasing levels of 3D shaping (Roberds *et al.* 2016). Our focus is on comparing a tokamak plasma with a stellarator configuration using new analysis tools. This section summarises experimental (Herfindal *et al.* 2019) and computational (Roberds *et al.* 2016) work that evaluates the effect of 3D shaping on sawtooth simulations in CTH.

The CTH vacuum vessel is circularly shaped with a minor radius $a = 0.3$ m and a major radius $R_o = 0.75$ m. The degree of 3D shaping is quantified by the amount of external rotational transform relative to the total transform, $h_{3D} = \iota_{\text{ext}}/(\iota_{\text{plasma}} + \iota_{\text{ext}})$ evaluated at the plasma edge. The value $h_{3D} = 0$ corresponds to a tokamak, in which the rotational transform is generated entirely by ohmically driven currents, whereas $h_{3D} = 1$ represents a current-free stellarator. Herfindal *et al.* (2019) have performed a systematic study of the effects of 3D shaping on CTH sawtooth oscillations by varying the fractional rotational transform in the $h_{3D} = 0.04$–0.42 range. The configurations have tokamak-like profiles for the safety factor, with an on-axis safety factor around unity that monotonically increases to an edge value between 1.6 and 5. The line-averaged electron density varies in the $n_e = 0.6$–$3.5 \times 10^{19}\,\text{m}^{-3}$ range and the peak plasma current in the range from 15 to 60 kA. In CTH, a typical value for the on-axis magnetic field is 0.5 T and for the electron temperature is 200 eV.

https://doi.org/10.1017/S0022377822000770 Published online by Cambridge University Press

Experiments report that the sawtooth oscillation frequency increases with the degree of 3D shaping. As measured from soft X-ray (SXR) emission of the plasma core, a sawtooth signal consists of a slow rise (the ramp-up phase) and a subsequent fast drop (the crash phase). However, there is no correlation between the crash time and the fractional rotational transform, and the increased sawtooth frequency can be attributed to a faster ramp-up.

Roberds *et al.* (2016) simulate sawtooth oscillations in CTH current-carrying stellarator using NIMROD (Sovinec *et al.* 2004). The plasma model consists of an MHD system of equations with Spitzer resistivity and anisotropic thermal conduction. Simulations are initialised with equilibria from the Variational Moments Equilibrium Code (VMEC) and are run by applying toroidal loop voltage at the plasma surface, which drives plasma currents typical in CTH. The role of 3D shaping is investigated by considering a set of four configurations with increasing values for the external rotational transform, $\iota_{\text{ext}} = 0.0, 0.0134, 0.0333$ and 0.0970. For these scenarios, approximate values for h_{3D} computed right after the first sawtooth crash are $h_{3D} \sim 0.0, 0.03, 0.07$ and 0.16.

The sawtooth frequency increase with 3D shaping has been retrieved from simulations of CTH. It is shown that the $n = 1$ energy grows faster for configurations with higher ι_{ext}, suggesting that equilibrium modifications lead to a faster linear growth rate. For all ι_{ext} cases, the linear growth rate is demonstrated to be proportional to $S^{-2/3}$, where S in the Lundquist number, which is in agreement with the linear growth rate of the resistive internal kink mode (Coppi *et al.* 1976; Ara *et al.* 1978).

3. Power-transfer analysis and the Lorentz power-transfer triad coefficients

This paper focuses on understanding the effect of 3D magnetic fields on the sawtooth instability. In a CTH's hybrid configuration, the stellarator fields modulate the energy transfer that drives the sawtooth instability. This section includes a recap of Ho & Craddock (1991) energy-transfer analysis tailored towards a generalisation for 3D geometry. The generalisation introduces the Lorentz power-transfer triad coefficients, which capture nonlinear interactions among Fourier modes, including those associated with stellarator fields.

The generalisation of the power-transfer analysis to a 3D equilibrium requires a consistent usage of the concepts of *linear eigenmode* and *toroidal Fourier mode*. A *linear eigenmode* is an eigenmode of the linearised extended MHD system of equations. Given (R, Z, φ) cylindrical coordinates, for a scalar field $g(R, Z, \varphi, t)$, the *toroidal Fourier mode* $g_n(R, Z, t)\mathrm{e}^{\mathrm{i}n\varphi}$ originates from the standard decomposition

$$g(R, Z, \varphi, t) = \sum_{n=-\infty}^{\infty} g_n(R, Z, t)\mathrm{e}^{\mathrm{i}n\varphi}. \tag{3.1}$$

The index n is the *toroidal mode number*. For a 3D vector field

$$\boldsymbol{g}(R, Z, \varphi, t) = g_R(R, Z, \varphi, t)\hat{\boldsymbol{e}}_R(\varphi) + g_Z(R, Z, \varphi, t)\hat{\boldsymbol{e}}_Z + g_\varphi(R, Z, \varphi, t)\hat{\boldsymbol{e}}_\varphi(\varphi), \tag{3.2}$$

a toroidal Fourier mode, $\boldsymbol{g}_n(R, Z, \varphi, t)\mathrm{e}^{\mathrm{i}n\varphi}$, results from the decomposition of each scalar component, so that

$$\boldsymbol{g}_n(R, Z, \varphi, t) = g_{R_n}(R, Z, t)\hat{\boldsymbol{e}}_R(\varphi) + g_{Z_n}(R, Z, t)\hat{\boldsymbol{e}}_Z + g_{\varphi_n}(R, Z, t)\hat{\boldsymbol{e}}_\varphi(\varphi). \tag{3.3}$$

For an axisymmetric equilibrium, a linear eigenmode is associated with a single toroidal mode number n; the internal $n = 1$ kink mode corresponding to a sawtooth instability in

https://doi.org/10.1017/S0022377822000770 Published online by Cambridge University Press

a tokamak is an example. In contrast, if the equilibrium possesses 3D features, a linear eigenmode has as projection onto multiple Fourier modes. In summary, n is a good quantum number when the equilibrium is axisymmetric (Spong 2015).

Toroidal Fourier modes are linearly coupled for a 3D equilibrium state, but they are not linearly coupled for an axisymmetric state (nonlinear effects couple Fourier modes in both cases). For a genuinely 3D equilibrium state with no symmetries whatsoever, linear coupling of the Fourier modes extends over the entire toroidal mode spectrum: $n = -\infty, \ldots, 0, \ldots, +\infty$. When the equilibrium possesses field-periodicity (as in CTH and other stellarators), the spectrum reduces to specific bands, known as mode families. A 3D equilibrium with a field period of N_{fp} can be expressed as a superposition of Fourier modes restricted to the toroidal mode numbers kN_{fp} for k an integer ($k \in \mathbb{Z}$). Likewise, the Fourier decomposition of a linear eigenmode for which $\boldsymbol{g}_n \neq 0$ (for some n) requires the superposition of all toroidal Fourier modes $\boldsymbol{g}_{n'}$ that satisfy the constraint $n' = n + kN_{\mathrm{fp}}$ for $k \in \mathbb{Z}$. CTH is a five-field period device ($N_{\mathrm{fp}} = 5$) and its banded structure consists of three families: a *symmetry-preserving* family, $n = kN_{\mathrm{fp}}$, and two *symmetry-breaking* ones, $n = kN_{\mathrm{fp}} \pm 1, kN_{\mathrm{fp}} \pm 2$. The internal kink linear eigenmode responsible for the sawtooth activity in CTH includes the complete $kN_{\mathrm{fp}} \pm 1$ family (Roberds *et al.* 2016), and not just the $n = 1$ toroidal Fourier mode, as in a tokamak. Henceforth, the $n = kN_{\mathrm{fp}} \pm 1$ family is referred to as the ± 1 fields, whereas the $n = kN_{\mathrm{fp}} \pm 2$ family is referred to as the ± 2 fields. In addition, when referring to the $n = \pm 5, \pm 10, \pm 15, \ldots$ Fourier modes, excluding $n = 0$, the terms *higher-order symmetry-preserving fields* or *stellarator fields* are used.

In this work, the power-transfer analysis is based upon assigning an energy content to each toroidal Fourier mode and quantifying the energy exchange between these modes. The standard definition of the total energy of a plasma involves an integral over internal, magnetic and kinetic energy density contributions:

$$E = \int_V \left(\frac{p}{\gamma - 1} + \frac{|\boldsymbol{B}|^2}{2\mu_o} + \frac{\rho |\boldsymbol{V}|^2}{2} \right) \mathrm{d}A \, \mathrm{d}\varphi. \tag{3.4}$$

Here, V is the confinement volume, $\mathrm{d}A$ is a poloidal cross-sectional differential of area and γ is the adiabatic constant (taken as $\gamma = 5/3$ in this work). To sort the total energy into contributions assigned to each toroidal mode, the starting point is to Fourier expand the pressure, magnetic, velocity and mass density fields in (3.4). During the evolution of the sawtooth simulations analysed in this work, non-axisymmetric Fourier mass density components (ρ_k, for $k \neq 0$) are smaller than its axisymmetric part (ρ_0). To leading order in the mass density, the plasma energy may be Fourier expanded as

$$E = \sum_n \int_V \left(\frac{p_n \mathrm{e}^{\mathrm{i}n\varphi}}{\gamma - 1} + \sum_q \left[\frac{\boldsymbol{B}_n \cdot \boldsymbol{B}_q^*}{2\mu_o} + \frac{\rho_0 \boldsymbol{V}_n \cdot \boldsymbol{V}_q^*}{2} \right] \mathrm{e}^{\mathrm{i}(n-q)\varphi} \right) \mathrm{d}A \, \mathrm{d}\varphi + O\left(\frac{\rho_k}{\rho_0} \right), \tag{3.5}$$

where superscript $*$ indicates a complex conjugate. The internal, magnetic and kinetic energy densities are linear, quadratic and cubic in the fields (p, ρ, $\boldsymbol{B}$ and $\boldsymbol{V}$), respectively. Accordingly, the Fourier mode decomposition of their constitutive fields leads to a single, a double and a triple sum, in that order. In (3.5), the triple sum originating from the kinetic energy density is a higher-order term, included in $O(\rho_k/\rho_0)$. During the toroidal integration of (3.5), only the $n = 0$ pressure component and the $q = n$ magnetic and kinetic terms survive. Toroidal integration yields the desired energy splitting:

$$E = \sum_n E_n + O\left(\frac{\rho_k}{\rho_0} \right). \tag{3.6}$$

https://doi.org/10.1017/S0022377822000770 Published online by Cambridge University Press

Here, the (leading-order) plasma energy associated with the nth Fourier mode is defined as an integral over the poloidal cross-section (A):

$$E_n = 2\pi \int_A \left(\frac{p_n}{\gamma - 1} \delta_{0,n} + \frac{|\boldsymbol{B}_n|^2}{2\mu_o} + \frac{\rho_0 |\boldsymbol{V}_n|^2}{2} \right) \mathrm{d}A. \tag{3.7}$$

The Kronecker delta $\delta_{0,n}$ ensures that the internal energy contributes only when $n = 0$. Note that the index n in E_n indicates that the integrand in (3.7) contains only the toroidal Fourier mode n of the fields p, $\boldsymbol{B}$ and $\boldsymbol{V}$.

A positive power transfer represents the addition of energy into a Fourier mode, which corresponds to mode growth, whereas a negative power transfer supports mode damping. For this reason, power transfers are used to track the Fourier mode energy time evolution. The power transfers that modify the internal, magnetic and kinetic Fourier mode energies are obtained from the time evolution equations. In this work, different energy types are lumped together into the Fourier mode energy (E_n in (3.7)); accordingly, the power transfers that determine the rate of change of the internal, magnetic and kinetic Fourier mode energies are combined into a single equation for the time evolution of E_n.

The Fourier mode energy time evolution is controlled by a competition between power-transfer contributions, each with concrete physical meaning. The governing equation for the time rate of E_n, and definite expressions for the power transfers, are given in appendix A. The Lorentz power (P_{L_n}) captures the nonlinear interaction among Fourier modes and, in particular, the current drive for instabilities. The resistive dissipation power (P_{η_n}) represents the dissipation due to a Spitzer resistivity that is fully dependent on position through the electron temperature. The Poynting flux (P_{PF_n}) is a conservative term that tracks energy flux across the plasma boundary; it captures the effect of the imposed loop voltage that drives CTH's ohmic currents. The viscous dissipation (P_{Π_n}) represents the power associated with the viscous stress tensor; it is negligible in this work. Additional power transfers are the pressure gradient ($P_{\nabla p_n}$) and the centre-of-mass advection (P_{A_n}).

The Lorentz power drives the sawtooth oscillation linear growth and it is the central quantity in our analysis. Its analytic expression,

$$P_{L_n} = 2\pi \int_A \boldsymbol{V}_n^* \cdot (\boldsymbol{J} \times \boldsymbol{B})_n \, \mathrm{d}A + 2\pi \int_A \boldsymbol{J}_n^* \cdot (\boldsymbol{V} \times \boldsymbol{B})_n \, \mathrm{d}A + \mathrm{c.c.}, \tag{3.8}$$

indicates that it is due to the $\boldsymbol{J} \times \boldsymbol{B}$ Lorentz force and the $\boldsymbol{V} \times \boldsymbol{B}$ induced electric field. In (3.8), c.c. indicates the complex conjugate of the previous terms. For conciseness, P_{L_n} is referred to as the *Lorentz power*. The Lorentz force drives the kinetic energy growth, whereas the induced electric field controls the evolution of the magnetic energy. Here P_{L_n} lumps together the Lorentz force and the induced electric field in the same way as E_n combines different energy types.

The terms $(\boldsymbol{J} \times \boldsymbol{B})_n$ and $(\boldsymbol{V} \times \boldsymbol{B})_n$ in (3.8) can be expanded as the sum

$$(\boldsymbol{A} \times \boldsymbol{B})_n = \sum_{n'} \boldsymbol{A}_{n'} \times \boldsymbol{B}_{n-n'}, \tag{3.9}$$

with $\boldsymbol{A} = \boldsymbol{J}$ or $\boldsymbol{A} = \boldsymbol{V}$. We define

$$\begin{aligned} f_{n,(n-n'),n'} = 2\pi \int_A \big\{ & \boldsymbol{V}_n^* \cdot (\boldsymbol{J}_{n'} \times \boldsymbol{B}_{n-n'}) + \boldsymbol{V}_n \cdot (\boldsymbol{J}_{n'}^* \times \boldsymbol{B}_{n-n'}^*) \\ & + \boldsymbol{J}_n^* \cdot (\boldsymbol{V}_{n'} \times \boldsymbol{B}_{n-n'}) + \boldsymbol{J}_n \cdot (\boldsymbol{V}_{n'}^* \times \boldsymbol{B}_{n-n'}^*) \big\} \, \mathrm{d}A, \end{aligned} \tag{3.10}$$

https://doi.org/10.1017/S0022377822000770 Published online by Cambridge University Press

so that

$$P_{L_n} = \sum_{n'} f_{n,(n-n'),n'}. \tag{3.11}$$

Note that the middle index in $f_{a,b,c}$ is the index of the magnetic field. The triad (or three-wave-coupling) coefficient $f_{n,(n-n'),n'}$ tracks the energy flowing into E_n due to fields with toroidal Fourier numbers n' and $n - n'$. Without further information, however, one does not know what portion of this energy flow comes from mode n' and what portion from mode $n - n'$. A direct calculation shows that $f_{n,(n-n'),n'} = -f_{n',(n'-n),n}$ implying that we can unambiguously interpret $f_{n,(n-n'),n'}$ as an energy flow from mode n' to mode n: the energy gained by mode n ($f_{n,(n-n'),n'}$) is lost by mode n' ($-f_{n',(n'-n),n}$). The magnetic field $\boldsymbol{B}_{n-n'}$ is unchanged by the interaction, and acts as a catalyst for the energy transfer between modes n' and n.

4. Magnetic field topology during sawtooth oscillations

This section expands the analysis of Roberds *et al.* (2016) by accurately tracking order-1 fixed points during sawtooth cycles. The analysis starts with an in-depth description of the first sawtooth cycle for the tokamak case ($t_{\text{ext}} = 0$), followed by a comparison of the tokamak versus the stellarator configurations. It is concluded that 3D shaping does not significantly modify the fixed-point picture of a sawtooth instability in a current-carrying stellarator.

4.1. *First sawtooth cycle: a prolonged initial instability growth and first crash*

Determining fixed points and associated quantities enables the study of topological changes in the magnetic field during sawtooth cycles. Early during the sawtooth cycle's ramp-up phase, the magnetic axis bifurcates into three fixed points, two o-points and an x-point. One o-point and the x-point correspond to the o-point and x-point of a newly formed magnetic island. The second o-point is the original magnetic axis. This bifurcation happens as the on-axis safety factor drops below unity and a $q = 1$ surface emerges. In Kadomtsev's theory, a growing $m = n = 1$ resistive internal kink causes the $q = 1$ surface to shrink and to expel energy to outer regions. The crash phase ends with the coalescence of the central o-point with the x-point, leaving the $m = n = 1$ island centre as the new magnetic axis and $q > 1$ everywhere. A temperature-dependent Spitzer resistivity leads to a subsequent current peaking in the core until $q_0 < 1$ again, restarting the cycle. This section analyses topological changes in the magnetic field by accurately tracking the position, safety factor and Greene's residue of all relevant fixed points during sawtooth oscillations of the tokamak simulation.

An accurate description of the topological changes during a sawtooth cycle requires an accurate determination of order-1 fixed points and their safety factors. This can be accomplished with a fixed-point finder algorithm such as that described by Hanson & Cary (1984). The algorithm tracks magnetic field lines via the return map, which follows the magnetic flow from one Poincaré surface back to the same surface. A fixed point of order n is defined as an invariant point of the map that results from applying the return map n times. These points can be determined to high accuracy using a Newton's method. The linearisation of the return map results in the tangent map, and the behaviour of the tangent map in the neighbourhood of a fixed point is described by either its eigenvalue or, equivalently, by its Greene's residue (Greene 1968, 1979). A Greene's residue (R_g) characterisation of the tangent map is physically advantageous. For example, the island width of a thin island is proportional to $\sqrt{R_g}$, where R_g is the Greene's residue of the island centre. More importantly, the Greene's residue of a fixed point and the safety factor

https://doi.org/10.1017/S0022377822000770 Published online by Cambridge University Press

at that location are related by $\cos(2\pi/q) = 1 - 2R_g$. In summary: during a sawtooth cycle order-1 fixed points are accurately determined using Newton's method and that is followed by the evaluation of their Greene's residues and safety factors.

Figure 1 shows the initial growth and two more sawtooth oscillations for the tokamak ($\iota_{\text{ext}} = 0$) simulation. This figure depicts a prolonged (∼3 ms) first cycle from 4.5 ms up to approximately 7.5 ms, followed by two shorter (∼0.5 ms) oscillations. Figure 1(*a*) shows the electron temperature measured at the initial location of the magnetic axis. Figure 1(*b*) illustrates the volume-integrated energy content of successively higher toroidal Fourier modes, as given by (3.7). Here $n = 0$ corresponds to the axisymmetric fields, whereas $n = 1$ is the growing internal kink responsible for the temperature crash. Figure 1(*c*) shows the safety factor of order-1 *o*-points. Figure 1(*d*) shows the major radius of fixed points at the $\varphi = 0$ plane. In this plane, the Z coordinates of the order-1 fixed points are very close to zero. Figure 1(*e*) gives the Greene's residue of these fixed points. The ramp-up phase of the first sawtooth cycle is bounded by the first and second vertical dashed lines; the first crash phase is bounded by the second and third vertical dashed lines. The determination of fixed points and related quantities allows to accurately specify the instants when q_0 crosses 1.

Initially (4.5 ms), the configuration possesses a set of good nested magnetic surfaces and a safety factor at the magnetic axis that is greater than unity ($q_0 = 1.01$ in figure 1*c*). As the simulation progresses, the magnetic axis safety factor (green line in figure 1*c*) decreases due to a peaking of the current profile in the less-resistive hotter core plasma. The Greene's residue (green line figure 1*e*) associated with the magnetic axis also decreases. This trend continues until 4.7 ms, when q drops below one, the residue drops to zero and a fixed-point bifurcation occurs (first dashed vertical line in figure 1). For a given *o*-point, its Greene's residue (R_g) and safety factor are related by $\cos(2\pi/q) = 1 - 2R_g$; $R_g = 0$ is consistent with $q = 1$. The emergence of a $q = 1$ surface is signaled by the bifurcation event that produces an *o*–*x* fixed-point pair. For $\varphi = 0$, figure 1(*d*) shows that the *o*-point (*x*-point) originates in the outboard (inboard) side of the poloidal cross-section.

The ramp-up phase begins at 4.7 ms and lasts until approximately 7.5 ms. The first indication of the resistive internal kink is the appearance of the *o*–*x* pair in the Greene's residue plot at 4.7 ms. In contrast, the $n = 1$ mode energy plot does not register the instability onset, and the mode growth is masked under numerical noise. The $n = 1$ growth in the energy is first seen at 5.7 ms. The residues for the *o*–*x* fixed-point pair remain at a numerical noise level of approximately 10^{-9} until 6.5 ms. During the ramp-up, the *o*–*x* fixed-point pair separate, indicating an expansion of the $q = 1$ surface.

The sawtooth crash begins just before 7.5 ms. First, we see that the electron temperature peaks at 7.43 ms (second vertical dashed line in figure 1). Then the $n = 1$ energy reaches a maximum at 7.55 ms. Shortly thereafter there is a bifurcation where the *o*–*x* fixed points coalesce at 7.58 ms (third vertical dashed line in figure 1). The coalescence is illustrated in figure 1(*d*) by the mutual destruction of a solid green trace with a dashed blue trace. After the coalescence, the centre of the growing island has become the new magnetic axis (red trace of figure 1*d*), and it is located roughly in the same position as the original magnetic axis. The fast electron temperature decrease and the subsequent reconnection process are known as the sawtooth crash. After the crash, the safety factor at the new magnetic axis is greater than unity (red trace in figure 1*c*). From then on, there is a sequence of sawtooth oscillations, and figure 1 displays two of them, from 7.6 to 8.6 ms.

4.2. *Tokamak and stellarator simulations: analogous fixed-point picture*

For the current-carrying stellarator simulations considered here, the 3D shaping has a small effect in the fixed-point picture of a sawtooth instability. Figure 2 compares sawtooth

https://doi.org/10.1017/S0022377822000770 Published online by Cambridge University Press

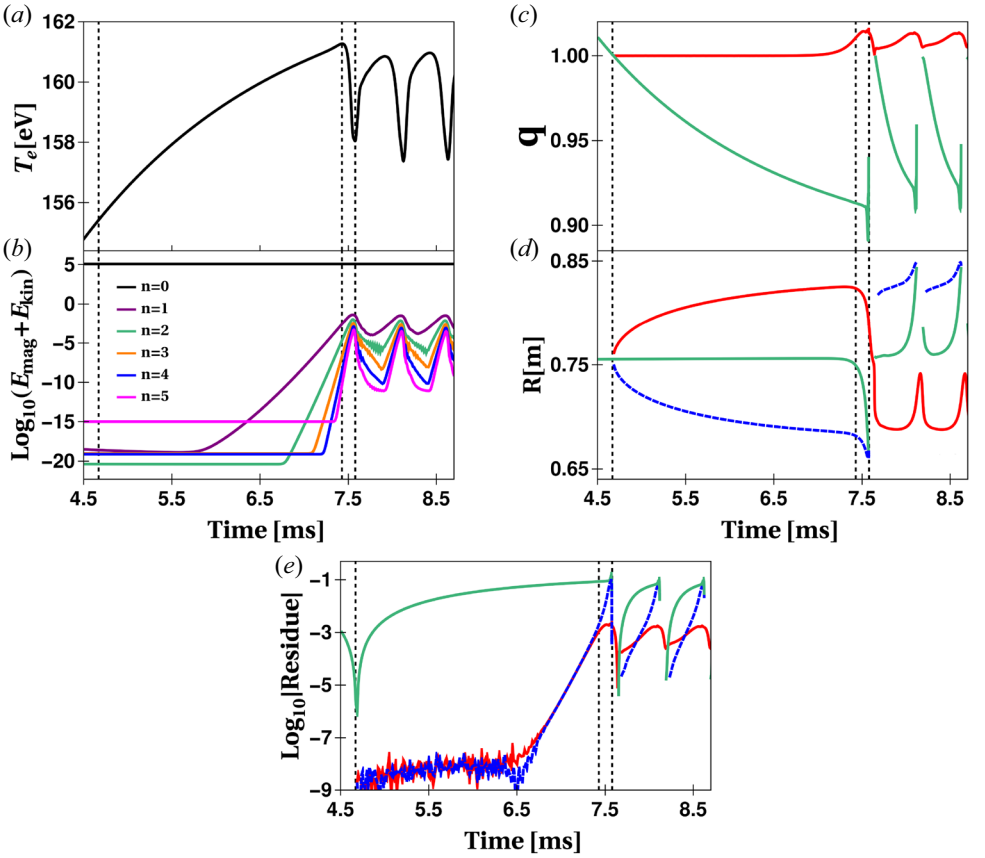

FIGURE 1. Sawtooth oscillations for a tokamak ($t_{\mathrm{ext}} = 0$). The simulation consists of a prolonged first cycle from 4.5 ms to approximately 7.5 ms, followed by a sequence of more frequent cycles. The panels correspond to (*a*) the electron temperature (T_e) at the location of equilibrium magnetic axis for $\varphi = 0$, (*b*) the volume integrated magnetic plus kinetic Fourier mode energies, (*c*) the safety factor, (*d*) the fixed-point R coordinate and (*e*) the Greene's residue. Panels (*c–e*) follow order-1 fixed points on the $\varphi = 0$ plane. Their Z coordinate is vanishingly small and is not shown. Red and green solid traces identify *o*-points, whereas dashed blue traces recognise *x*-points. Blue traces do not appear in panel (*c*), as the safety factor is undefined for *x*-points. The ramp-up phase of the first sawtooth cycle is bounded by the first and second vertical dashed lines; the crash phase is bounded by the second and third vertical dashed lines.

cycles for a stellarator configuration ($t_{\mathrm{ext}} = 0.0333$) with the tokamak scenario ($t_{\mathrm{ext}} = 0$). The time window is centred around the second sawtooth cycle for both cases, and the time coordinate is shifted by the instant when the first coalescence occurs ($t_{\mathrm{saw}} = \mathrm{Time} - T_{\mathrm{first\ coalescence}}$). For example, $T_{\mathrm{first\ coalescence}} = 7.58$ ms for the tokamak simulation (shortly after the third dashed vertical line in figure 1). In figure 2, four vertical dashed lines bound regions where $q_0 > 1$ and $q_0 < 1$. The discussion is complemented with Poincaré plots through the sawtooth cycle in figure 3.

The tokamak and the stellarator quantities given in figure 2 at $t_{\mathrm{saw}} = 0$ (first vertical dashed line) are similar. Both configurations have a monotonically decreasing on-axis safety factor of approximately $q_0 \sim 1.02$ (red traces in figure 2*c*,*h*). Around this time, there is a local minimum in the electron temperature (figure 2*a*,*f*), maximum energy stored in

https://doi.org/10.1017/S0022377822000770 Published online by Cambridge University Press

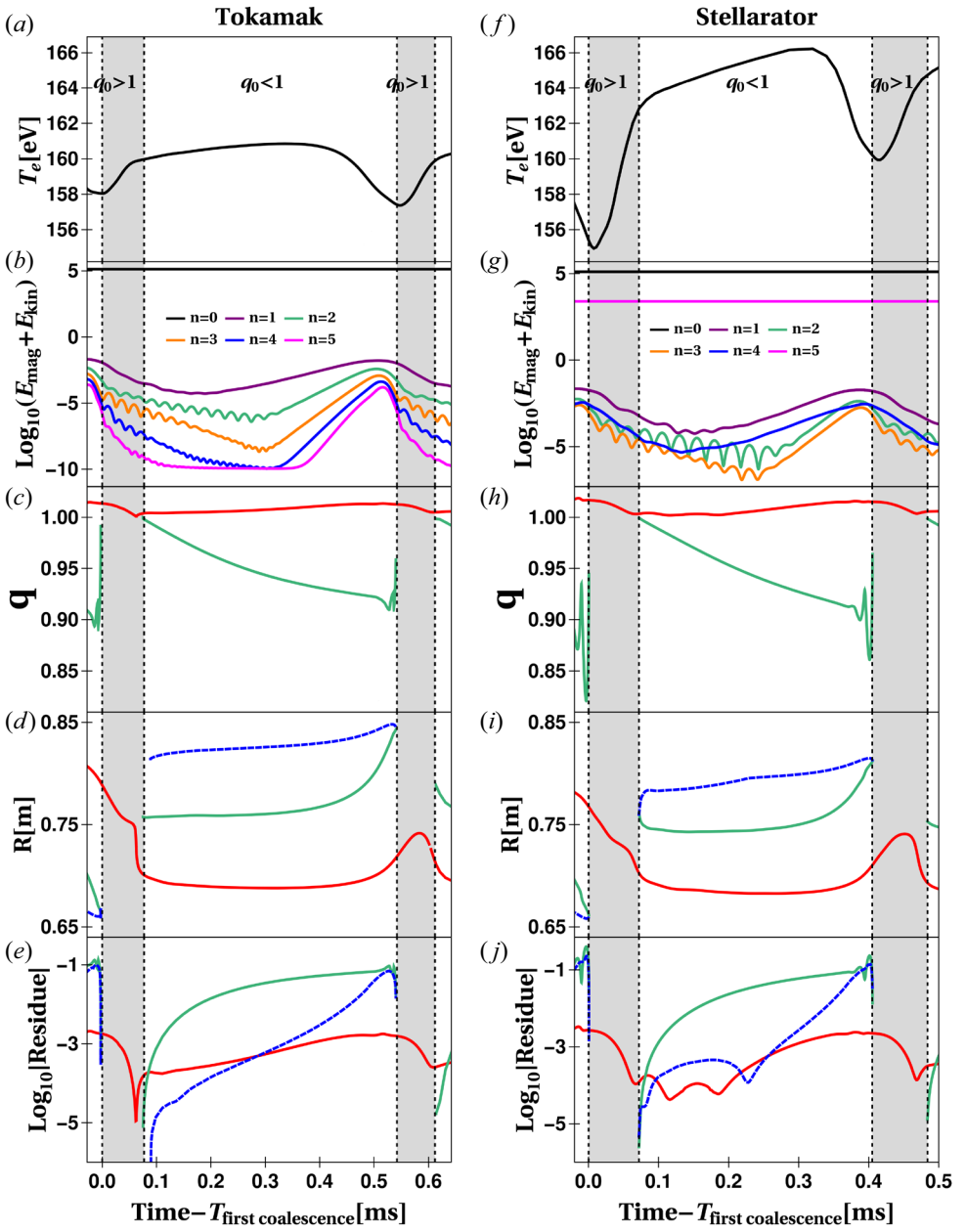

FIGURE 2. Sawtooth oscillations for a tokamak ($t_{\mathrm{ext}} = 0$) and a stellarator ($t_{\mathrm{ext}} = 0.0333$). To facilitate the comparison, we have shifted the time by the instant when the first *o*–*x* coalescence occurs (right after the initial sawtooth cycle). (*a*,*f*) Electron temperature; (*b*,*g*) magnetic plus kinetic Fourier mode energies; (*c*,*h*) the safety factor at the fixed-point location; (*d*,*i*) fixed-point R coordinate on the $\varphi = 0$ plane; (*e*,*j*) the absolute value of the Greene's residue. In panels (*d*,*e*,*i*,*j*), the dashed blue curves correspond to *x*-points whereas the solid curves correspond to *o*-points. The vertical dashed lines limit the regions where the on-axis safety factor is greater or smaller than unity.

https://doi.org/10.1017/S0022377822000770 Published online by Cambridge University Press

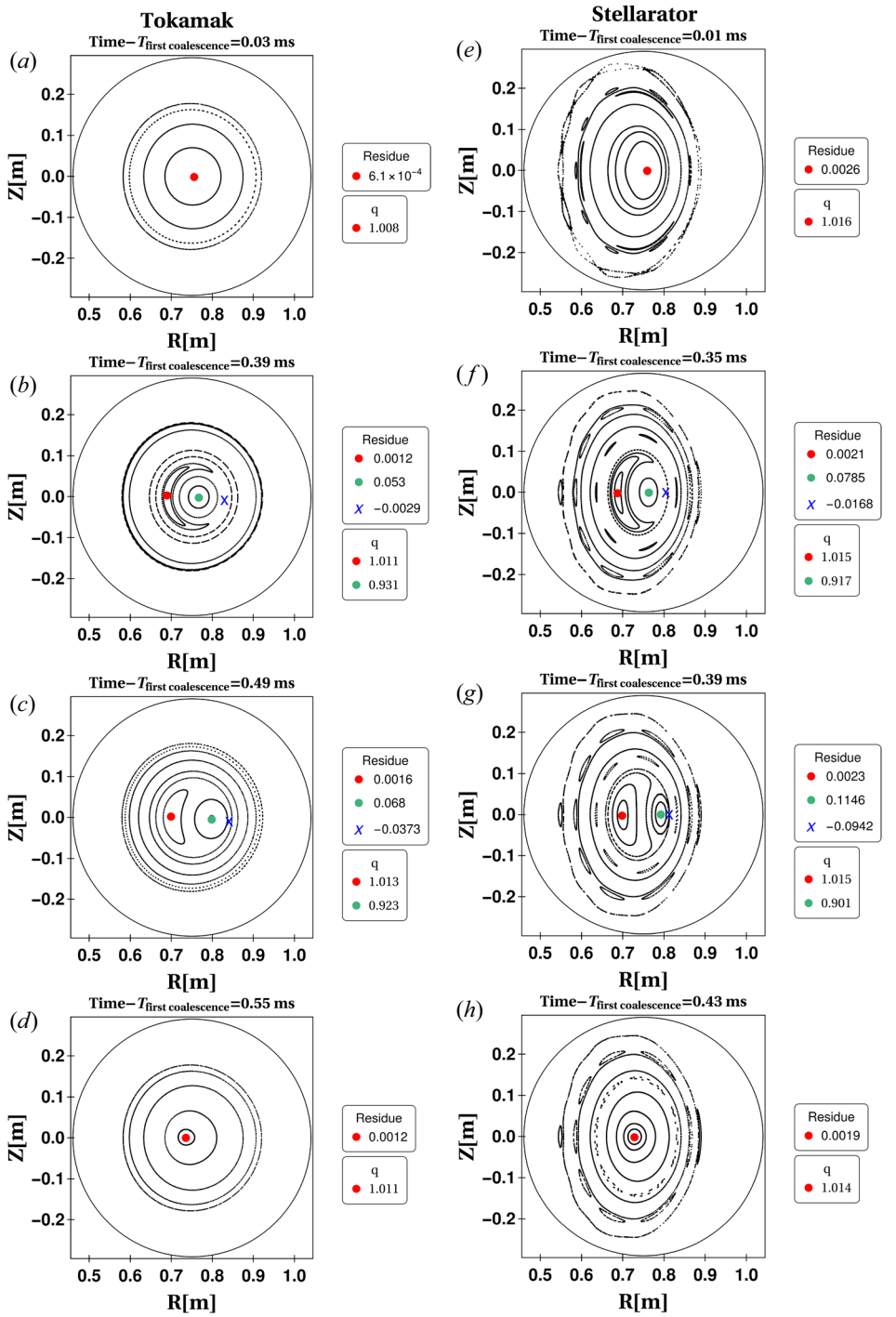

FIGURE 3. Poincaré surface of sections during sawtooth oscillations for (*a–d*) a tokamak ($t_{\text{ext}} = 0$) and (e–h) a stellarator ($t_{\text{ext}} = 0.0333$) at the $\varphi = 0$ plane. (*a*,*e*) On-axis q is larger than one. (*b*,*f*) On-axis q has dropped below unity. The $q = 1$ surface emergence is recognised by the newly created central *o*-point (green dot) and *x*-point (blue *x*). (*c*,*g*) As the internal kink mode grows, the magnetic axis is pushed towards the *x*-point. (*d*,*h*) The reconnection process has been completed, and the centre of the growing island has become the new magnetic axis.

https://doi.org/10.1017/S0022377822000770 Published online by Cambridge University Press

non-axisymmetric fields (figure 2*b*,*g*), and vanishing residues for the magnetic axis and the reconnection point of the previous sawtooth cycle (green and blue traces in figure 2*e*,*j*). Tokamak and stellarator Poincaré plots at 0.03 ms and 0.01 ms are given in figures 3(*a*) and 3(*e*), respectively. The tokamak case shows circular nested flux surfaces. The stellarator case shows elongated nested surfaces with symmetry-preserving 6/5 and 8/5 island chains.

The $q = 1$ surfaces emerge at $t_{saw} \sim 0.07$ ms in tokamak and stellarator simulations. This is indicated by the bifurcation event that produces an o–x fixed-point pair at the second vertical dashed line in both the R coordinate plot (blue and green traces in figure 2*d*,*i*) and the residues plot (blue and green traces in figure 2*e*,*j*). The red traces of figure 2(*d*,*i*) at $t_{saw} \sim 0.07$ ms show that the original magnetic axis is displaced towards the inboard side due to the formation of a $q = 1$ surface in the core. Furthermore, the original magnetic axis's safety factor retains a value greater than unity through this event (red traces in figure 2*c*,*h*). The tokamak and stellarator Poincaré plots in figures 3(*b*) ($t_{saw} = 0.39$ ms) and 3(*f*) ($t_{saw} = 0.35$ ms) confirm that the bifurcation process has effectively transformed the original magnetic axis into a magnetic island centre (red dot). In these plots, the newly created central o-point is marked by a green dot and the x-point by a blue x. The bifurcation dynamics in the first 10 μs after q crosses unity is more complicated than the simplified picture presented here. This is examined in more detail in appendix B, but has minimal effect on the longer time scale sawtooth dynamics.

Sawtooth crashes for the tokamak and stellarator cases occur at $t_{saw} \sim 0.54$ ms and $t_{saw} \sim 0.41$ ms, respectively. Poincaré plots before ($t_{saw} = 0.49$ ms) and after ($t_{saw} = 0.55$ ms) the tokamak sawtooth crash are given, respectively, in figures 3(*c*) and 3(*d*). Similarly, figure 3(*g*,*h*) show Poincaré plots before ($t_{saw} = 0.39$ ms) and after ($t_{saw} = 0.43$ ms) the crash for the stellarator case. The temperature crash (figure 2*a*,*f*) is due to the displacement of the hot core towards the reconnection point during the coalescence event. As the magnetic island grows, it pushes the recently created o-point towards the x-point, which drives the reconnection process. This process is portrayed in figure 2(*d*,*i*) as green and blue traces merging around the third vertical dashed line.

The fixed-point picture during sawtooth cycles is mostly unchanged by the application of a stronger external rotational transform. This analysis has also been performed for the $\iota_{ext} = 0.0133$ and 0.0970 cases considered by Roberds *et al.* (2016) and the fixed-point picture is consistent throughout. The decrease of the sawtooth period for increased levels of 3D shaping has been experimentally observed (Herfindal *et al.* 2019) and computationally verified (Roberds *et al.* 2016). Despite some well-understood particularities during the $q = 1$ surface emergence (appendix B), the tokamak and stellarator simulations are described by Kadomtsev's model.

5. Power transfer in a 3D geometry

Although 3D shaping does not affect the sawtooth fixed-point picture, there are differences between the tokamak and stellarator simulations in how the sawtooth instability is driven. Section 2 highlights that the sawtooth frequency increases with 3D shaping; it also points out that part of this variation is explained in terms of an increased growth rate during the linear phase. This section focuses on the power transfer that drives the sawtooth instability in the linear phase for the tokamak and the stellarator cases. The nonlinear saturation and crash phases are discussed briefly. We find that the stellarator fields have two competing effects on the linear kink instability. First, the stellarator fields remove energy from the kink, which is stabilising. Second, the stellarator fields catalyse energy transfer from large-to-small scales. We conjecture that this transfer of energy to small scales effectively enhances the reconnection rate, which would increase the linear growth rate.

https://doi.org/10.1017/S0022377822000770 Published online by Cambridge University Press

The internal kink linear eigenmode in a stellarator configuration consists of coupled toroidal Fourier modes. In a tokamak, the equilibrium is characterised by $n = 0$; in contrast, the stellarator equilibrium encompasses the symmetry-preserving family ($n = 0, \pm 5, \pm 10, \ldots$). For the tokamak, the internal kink linear eigenmode is identified with $n = 1$. In the stellarator, $n = 1$ toroidally couples with all the $kN_{\mathrm{fp}} \pm 1$ fields. Figure 2 shows the evolution of Fourier mode energies for the tokamak (figure 2*b*) and stellarator (figure 2*g*) simulations. The linear growth phase for the tokamak case occurs from $\sim$0.2 to $\sim$0.4 ms; the linear growth phase for the stellarator case occurs from $\sim$0.2 to $\sim$0.35 ms. For the tokamak in the linear growth phase, the $n = 1$–4 mode energies are at successively lower values, with successively higher growth rates. In contrast, for the stellarator case, the $n = 1$ and 4 modes grow at the same rate, and the $n = 2$ and 3 mode energies are at a lower energy and grow at a higher rate than the $n = 1$ and 4 modes. In the stellarator case, the internal kink linear eigenmode has a finite projection onto the ± 1 fields, and vanishing projection onto the remaining Fourier modes.

Figure 4 shows the energy evolution of the extended Fourier spectrum for the stellarator simulation. Figures 4(*a*)–4(*c*) show the energy of symmetry-preserving fields, ± 1 fields and ± 2 fields, respectively. The energy in each symmetry-preserving field ($n = kN_{\mathrm{fp}}$) is constant in time, with energy decreasing with higher n. These energies are predominately magnetic field energy and are approximately seven orders of magnitude larger than the symmetry-breaking modes with similar n values. The ± 1 modes show a characteristic linear growth phase, the log energy increasing linearly in time at the same rate, and the total energy decreasing with increasing n. The ± 2 modes are at smaller amplitude than nearby ± 1 modes. Toward the end of the linear growth phase, the ± 2 mode energies all show exponential growth, with a faster growth rate than the ± 1 modes. This is consistent with the fact that the ± 2 modes are driven nonlinearly by ± 1 mode interaction. During the linear growth phase, the energy evolution is dominated by the linear eigenmode growth. Thus, we use the ± 1 modes as a proxy for the linearly growing eigenmode. We note that the higher n modes growth rate begins to increase towards the end of this phase, which indicates that the linear approximation, or the assumption that the ± 1 Fourier modes are a good proxy for the eigenmode, is beginning to break down.

The Lorentz power drives the growth during the linear phase, as can be seen in figure 5. This figure shows the power transfers for the tokamak $n = 1$ (figure 5*a*), stellarator $n = 1$ (figure 5*b*) and stellarator $n = 4$ (figure 5*c*). In all three cases, the total power transfer and the Lorentz power transfer are nearly identical during the linear growth phase, and the other power transfers (pressure gradient, resistive dissipation and advective) are negligibly small. The other power transfers become important once the x and o points coalesce (at the third vertical dashed line).

To further understand the Lorentz power during sawtooth cycles, it is convenient to consider energy-transfer rates between specific Fourier modes. As explained in § 3, $f_{n,(n-n'),n'}$ is the Lorentz energy transfer rate from $E_{n'}$ to E_n catalysed by $\boldsymbol{B}_{n-n'}$. The $f_{n,(n-n'),n'}$ coefficients for the tokamak and stellarator cases are plotted in figures 6(*a*)–6(*c*) and 6(*d*)–6(*f*), respectively. Figures 6(*a*) and 6(*d*) correspond to times right after the crash, but before q_0 drops below unity again, figures 6(*b*) and 6(*e*) are for times during the linear phase, and figure 6(*c*) and 6(*f*) are near saturation, shortly before the next crash. As the coefficients cover multiple orders of magnitude, figure 6 uses a logarithmic scale. For a given n, the Lorentz power P_{L_n} is obtained by summing over all matrix elements in the nth column.

Several properties of the Lorentz power-transfer coefficients are reflected in the structure of the plots in figure 6. (i) The conservation of energy antisymmetry ($f_{n,(n-n'),n'} = -f_{n',(n'-n),n}$) implies that the Lorentz power-transfer coefficients are the same, save for

https://doi.org/10.1017/S0022377822000770 Published online by Cambridge University Press

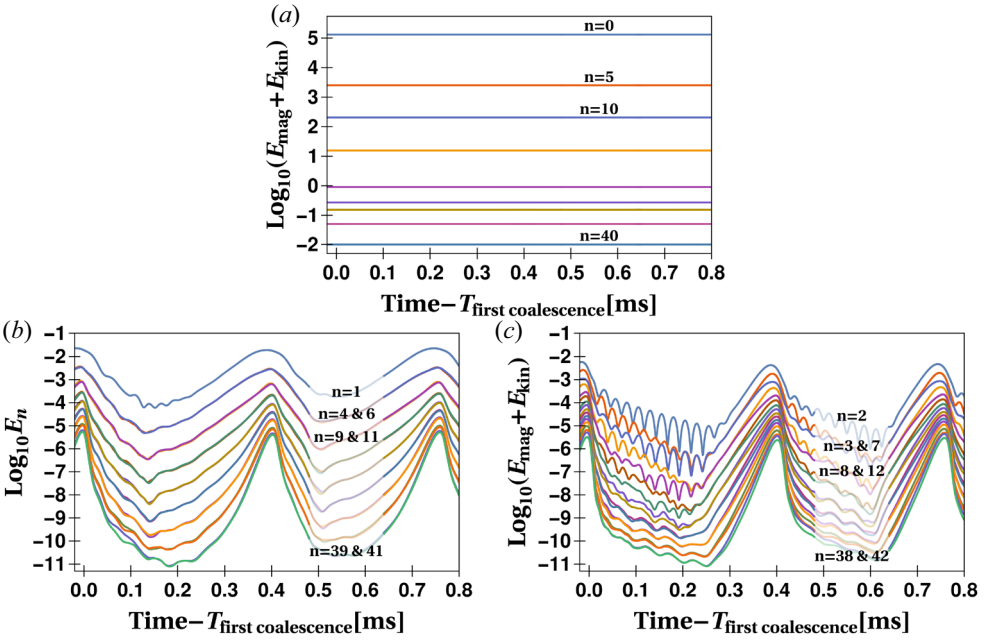

FIGURE 4. Magnetic plus kinetic Fourier mode energies for the stellarator ($t_{\text{ext}} = 0.0333$) simulation: (*a*) symmetry-preserving modes; (*b*) ± 1 Fourier modes; (*c*) ± 2 Fourier modes. Note that panel (*a*) has a different energy scale than panels (*b*,*c*). The energy content of a given $+n$ field is equal to that of the energy content of $-n$, so only half on them are shown.

a sign change, upon reflection across the $n = n'$ line. (ii) The $n = n'$ diagonal is zero, because there is no energy transfer of a Fourier mode to itself. (iii) Fourier modes of real fields obey a complex conjugate symmetry (e.g. $\boldsymbol{B}_n = \boldsymbol{B}^*_{-n}$). This property implies that the plots are invariant under inversions through the origin: $f_{n,(n-n'),n'} = f_{-n,(n'-n),-n'}$. The physical implication is that the Lorentz power transfer from $E_{n'}$ to E_n is equal to that from $E_{-n'}$ to E_{-n}. (iv) The conservation of energy antisymmetry and the complex conjugate symmetry, in turn, imply that the coefficients change sign when reflected across the $n = -n'$ line, i.e. $f_{n,(n-n'),n'} = -f_{-n',(n-n'),-n}$. The interpretation is that the power transfer from $E_{n'}$ to E_n is the negative of that from E_{-n} to $E_{-n'}$. (v) From the preceding condition, it follows that the coefficients along the $n = -n'$ line vanish ($f_{-n,(-2n),n} = 0$). This is expected: the Lorentz power coefficients modify the magnetic and kinetic Fourier mode energies, and these quantities are proportional to $|\boldsymbol{B}_n|^2 = \boldsymbol{B}_n \cdot \boldsymbol{B}_{-n}$ and $|\boldsymbol{V}_n|^2 = \boldsymbol{V}_n \cdot \boldsymbol{V}_{-n}$, respectively, i.e. the energies are constructed from Fourier modes with indices n and $-n$. (vi) It is seen that figure 6 can be recovered through reflections and transpositions from, say, the upper wedge ($n' > |n|$). The remaining matrix entries are redundant.[1]

CTH's five-fold toroidal periodicity imposes a structure in the power-transfer matrix for the stellarator simulation. For this simulation, the symmetry-preserving Fourier modes $\boldsymbol{B}_{5k}$ are the largest of the magnetic field Fourier modes. Their catalytic effect is quantified by the $f_{n,(5k),n-5k}$ coefficients, located along the $n' = n + 5k$ lines in figures 6(*d*)–6(*f*). Along these lines, the $f_{5n,5(n-n'),5n'}$ entries are local extrema. These coefficients correspond

[1]The power axis uses a signed-log scale. For a given positive number p, the scale is linear in between $-p \le x \le p$, maps to $\log(x/p) + p$ for $x > p$ and to $-\log(|x|/p) - p$ for $x < -p$. In figures 5 and 6, $p = 10$ W. In figures 7 and 8, $p = 1$ W.

https://doi.org/10.1017/S0022377822000770 Published online by Cambridge University Press

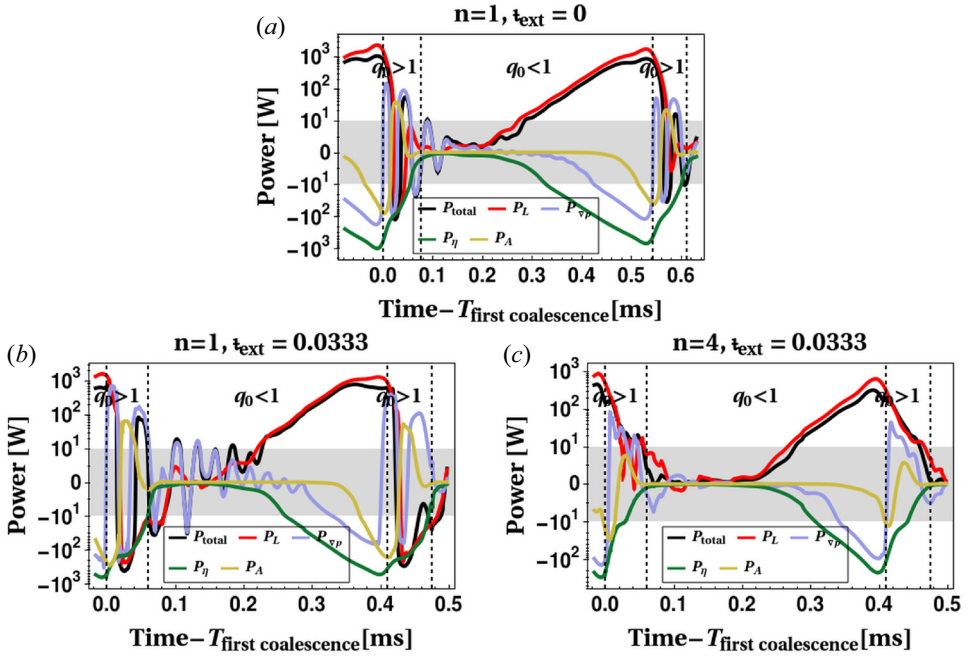

FIGURE 5. Power-transfer contributions during the first sawtooth oscillation: (*a*) tokamak $n = 1$; (*b*) stellarator $n = 1$; (*c*) stellarator $n = 4$. The power scale is linear within the grey area and logarithmic elsewhere[1]. The vertical dashed lines limit the regions where the on-axis safety factor is greater or smaller than unity. The first and third vertical lines correspond to fixed-point coalescences during sawtooth crashes, the second and fourth vertical lines correspond to bifurcations of the magnetic axis as the on-axis safety factor drops below unity.

to power transfers catalysed by symmetry-preserving fields exclusively. An example of an interaction of this class is the $f_{5,(5),0}$ coefficient, corresponding to power transfer from $n' = 0$ to $n = 5$. This coefficient is the global maximum of figure 6(*d*), early during the cycle, and of figure 6(*f*), right before the crash. The following discussion explores ways in which the $\boldsymbol{B}_{5k}$ symmetry-preserving Fourier modes modulate the sawtooth growth.

In the tokamak case, the $n = 1$ resistive internal kink grows by taking energy from $n' = 0$. The $f_{1,(1),0}$ entry in figures 6(*a*)–6(*c*) captures this interaction. These figures show that $f_{1,(1),0}$ increases during the cycle. In a tokamak, the coefficients that drive the linear growth peak around the origin ($n = n' = 0$).

In the stellarator case, we use the ± 1 Fourier modes as a proxy for the linearly growing kink eigenmode. Energy flow into and within the eigenmode is given by

$$P_{\text{eigen}} = \sum_{n=kN_{\text{fp}}\pm 1} \sum_{n'} f_{n,(n-n'),n'}. \tag{5.1}$$

We separate the n' indices into four disjoint groups: (i) $n' = jN_{\text{fp}}$, energy transfer into the eigenmode from symmetry-preserving fields; (ii) $n' = jN_{\text{fp}} \pm 2$, energy transfer into the eigenmode from ± 2 fields; (iii) $n' = jN_{\text{fp}} \pm 1$ and $n - n' = lN_{\text{fp}}$, energy rearrangement within the eigenmode catalysed by symmetry-preserving fields; (iv) $n' = jN_{\text{fp}} \pm 1$ and $n - n' = lN_{\text{fp}} \pm 2$, energy rearrangement within the eigenmode catalysed by ± 2 fields. Here, j and l are integers. Groups (i) and (ii) quantify energy transfer into the eigenmode

https://doi.org/10.1017/S0022377822000770 Published online by Cambridge University Press

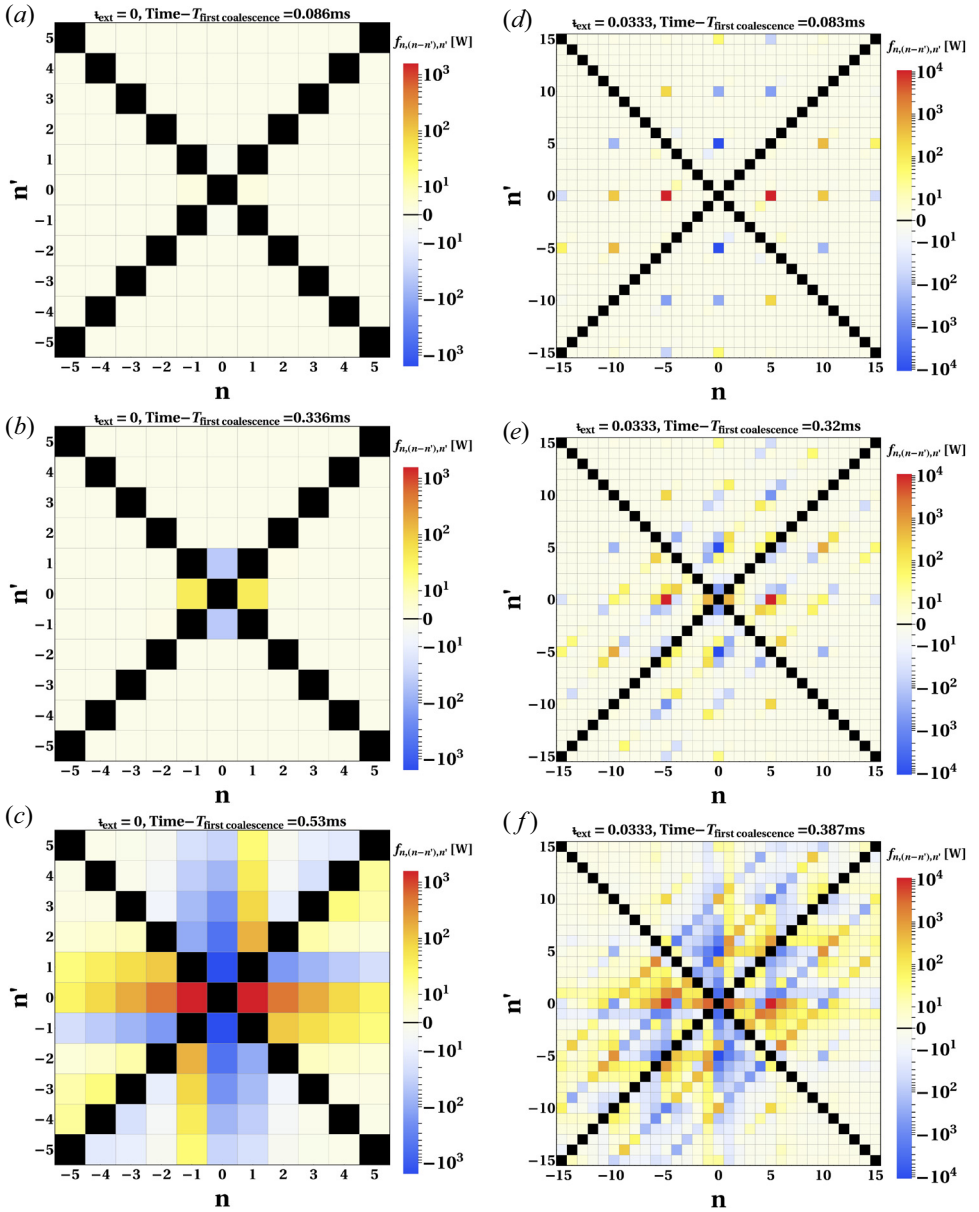

FIGURE 6. Lorentz power-transfer triad coefficients during the sawtooth cycle for the (*a–c*) tokamak ($t_{ext} = 0$) and (d–f) stellarator ($t_{ext} = 0.0333$). Panels (*a*,*d*) correspond to times after the crash, but before q_0 drops below unity again, (*b*,*e*) are for times during the linear phase, (*c*,*f*) correspond to times near the saturation, shortly before the next crash. Note the different colour scales and axis range for each configuration. The power scale is linear in the −10 to 10 W range and logarithmic elsewhere.

from Fourier modes not belonging to the eigenmode itself. Groups (iii) and (iv) quantify energy rearrangement within the eigenmode.

Figure 7 shows the Lorentz power transfer into (but not within) the kink eigenmode from the whole Fourier spectrum. That is, the n' values included in the sum are those described in groups (i) and (ii). In addition to plotting the total flow in, the figure also

https://doi.org/10.1017/S0022377822000770 Published online by Cambridge University Press

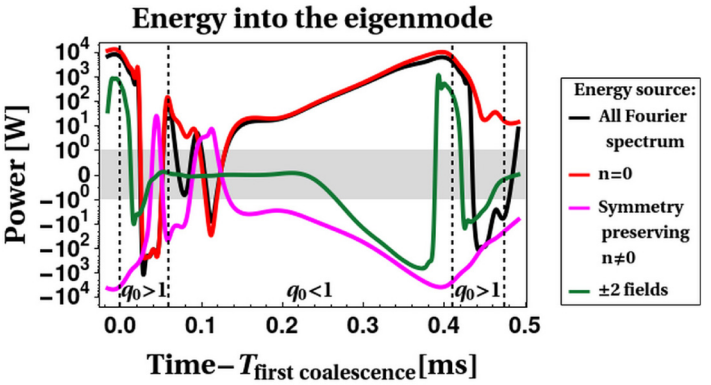

FIGURE 7. Stellarator simulation ($t_{\text{ext}} = 0.0333$). Lorentz power transfer into the kink eigenmode from the whole Fourier spectrum, the $n = 0$ field, the stellarator fields ($n = \pm 5, \pm 10, \pm 15, \ldots$) and the ± 2 fields ($n = \pm 2, \pm 3, \pm 7, \ldots$). The power scale is linear within the grey area and logarithmic elsewhere.

shows the individual contributions from the axisymmetric fields ($n' = 0$), the stellarator fields ($n' = kN_{\text{fp}}$), and the ± 2 fields ($n' = kN_{\text{fp}} \pm 2$). During the linear growth phase, the power from the whole Fourier spectrum is approximately equal to the transfer from the axisymmetric fields. The transfer from the ± 2 fields is negligible, and the transfer from the stellarator fields is small and negative. The stellarator fields *remove* energy from the eigenmode. Thus, they are not a source of free energy that drives growth.

The Lorentz power transfer within the kink eigenmode can be expressed in sums of the form of (5.1), with n' in the groups (iii) (energy rearrangement catalysed by symmetry-preserving fields) or (iv) (energy catalysed by ± 2 fields). However, the complete sum in (5.1) with all n' in group (iii) or all n' in group (iv) gives zero. Every contribution describing flow from n' to n is cancelled by the energy flow from n to n'. To clarify what is happening with the energy flow within the eigenmode, we add a condition to the sum: that $|n| > |n'|$. With this condition, the sum only includes the power flow from small $|n'|$ to large $|n|$ (large scale to small scale):

$$P_{\text{up}} = \sum_{n=kN_{\text{fp}}\pm 1} \sum_{n'=lN_{\text{fp}}\pm 1 \text{ and } |n|>|n'|} f_{n,(n-n'),n'}. \tag{5.2}$$

Note that the sign of P_{up} and f can both be positive or negative. If positive, the energy is flowing from large-to-small scales. If negative the energy is flowing from small-to-large scales.

Figure 8 shows the large-to-small scales energy rearrangement within the eigenmode catalysed by the stellarator fields ($n - n' = \pm 5, \pm 10, \pm 15, \ldots$), ± 2 fields ($n - n' = \pm 2, \pm 3, \pm 7, \ldots$) and by the field pairs $\boldsymbol{B}_{\pm 5}$, $\boldsymbol{B}_{\pm 10}$ and $\boldsymbol{B}_{\pm 15}$. This figure shows that the large-to-small scales energy rearrangement within the eigenmode catalysed by the stellarator fields is positive during the linear phase while there is a negligible catalytic effect of the ± 2 fields. The implication is that the higher-order Fourier modes of the kink eigenmode grow at the expense of energy catalysed by the stellarator fields from large-to-small scales.

Figure 8 also shows that the large-to-small scales energy rearrangement within the eigenmode catalysed by the stellarator fields is mainly due to the catalytic effect of $\boldsymbol{B}_{\pm 5}$ and $\boldsymbol{B}_{\pm 10}$. The forward cascade catalysed by $\boldsymbol{B}_{-5}$ and $\boldsymbol{B}_{5}$ are equal and figure 8 shows

https://doi.org/10.1017/S0022377822000770 Published online by Cambridge University Press

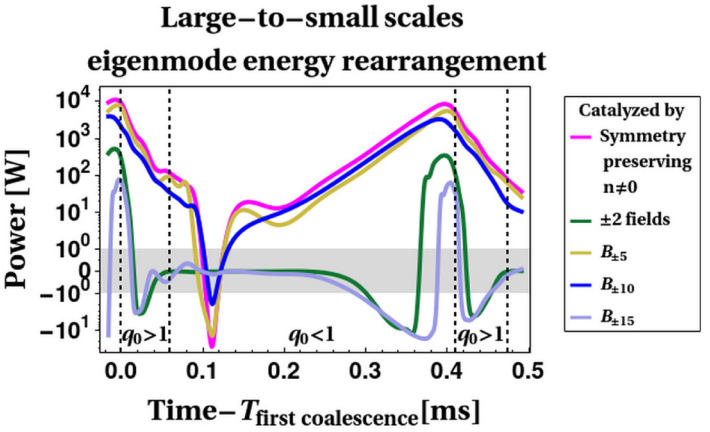

FIGURE 8. Stellarator simulation ($t_{\text{ext}} = 0.0333$). Large-to-small scales energy rearrangement within the eigenmode catalysed by the stellarator fields ($n = \pm5, \pm10, \pm15, \ldots$), ±2 fields ($n = \pm2, \pm3, \pm7, \ldots$), $\boldsymbol{B}_{\pm5}$, $\boldsymbol{B}_{\pm10}$ and $\boldsymbol{B}_{\pm15}$. The power scale is linear within the grey area and logarithmic elsewhere.

their sum. The same observation applies for the $\boldsymbol{B}_{\pm10}$ and $\boldsymbol{B}_{\pm15}$ pairs. The $\boldsymbol{B}_{\pm5}$ and $\boldsymbol{B}_{\pm10}$ fields have a comparable catalytic role during the linear phase that rearranges, within the eigenmode, energy from large scales to small scales. Unexpectedly, the catalytic effect of $\boldsymbol{B}_{\pm5}$ is of the same order of magnitude as that of $\boldsymbol{B}_{\pm10}$. The catalytic effect of $\boldsymbol{B}_{\pm15}$ is orders of magnitude smaller than that of $\boldsymbol{B}_{\pm5}$ and $\boldsymbol{B}_{\pm10}$. The smallness is expected from the ordering of the symmetry-preserving fields.

Figure 8 highlights that stellarators fields rearrange energy within the kink eigenmode through a forward cascade. The forward cascade transfers energy from large scales to small scales, and magnetic reconnection is stronger at smaller length scales. It is hypothesised that this energy catalysis results in an increased reconnection rate. This hypothesis is consistent with the observed increase in the resistive kink growth rate with increasing stellarator fields reported in Roberds *et al.* (2016), and it is consistent with experimental trends (Herfindal *et al.* 2019).

6. Discussion and conclusions

This paper revisits sawtooth NIMROD simulations of CTH operating as a tokamak and as a current-carrying stellarator. The analysis employs a new fixed-point finder for NIMROD post-processing and adapts the power-transfer analysis of Ho & Craddock (1991) to explore a 3D equilibrium.

This work determines that the fixed-point picture during sawtooth oscillations in CTH's tokamak and stellarator scenarios are similar. The fixed-point analysis allows for a detailed description of the sawtooth cycle. (i) During the initial sawtooth oscillation for the tokamak case, the first indication of the kink eigenmode onset is the bifurcation of the magnetic axis into an $n = m = 1$ magnetic island centre and reconnection point (as shown in the Greene's residue plot) rather than the growth of the sawtooth energy content (which is masked under numerical noise). (ii) The accurate determination of fixed points, safety factors and residues resulted in the identification of two fixed-point mechanisms during the emergence of the internal kink, as shown in (appendix B).

The Lorentz power transfer is the internal kink eigenmode driver for the tokamak and the stellarator cases. Surprisingly, stellarator fields damp the sawtooth instability's

https://doi.org/10.1017/S0022377822000770 Published online by Cambridge University Press

linear growth. The primary role of stellarator fields is to catalyse energy transfer from large-to-small scales within the eigenmode. The aforementioned forward cascade may be related to the increased linear growth with 3D shaping, as reported by Herfindal *et al.* (2019) and Roberds *et al.* (2016). This is a topic of future work.

An important consequence of the generalisation of Ho & Craddock (1991) analysis to a 3D equilibrium is the introduction of the Lorentz power-transfer triad coefficients $f_{n,(n-n'),n'}$. The coefficient can be interpreted as an energy flow from mode n' to mode n catalysed by the magnetic field $\boldsymbol{B}_{n-n'}$. The collection of coefficients for CTH's stellarator scenarios has an underlying structure imposed by the $N_{\mathrm{fp}} = 5$ field-periodicity. These coefficients may prove fruitful for analysing sawtooth or other MHD activity in generic stellarators. The power-transfer analysis makes no β assumptions and may be employed for configuration with arbitrary cross-sectional geometry. The Lorentz power-transfer triad coefficients can be used to quantify symmetry-breaking effects in tokamaks, such as those produced by 3D fields for edge localized mode (ELM) suppression.

Acknowledgements

O.E.L. would like to acknowledge the assistance of J.R. King and S.E. Kruger.

Editor Per Helander thanks the referees for their advice in evaluating this article.

Funding

This work was supported by US Department of Energy Grant Nos. DE-FG02-03ER54692, DE-SC0018313 and DE-FG-02-00ER54610. This research used resources of the National Energy Research Scientific Computing Center (NERSC), a US Department of Energy Office of Science User Facility located at Lawrence Berkeley National Laboratory, operated under Contract No. DE-AC02-05CH11231. This manuscript has been authored in part by UT-Battelle, LLC, under contract DE-AC05-00OR22725 with the US Department of Energy (DOE). The US government retains and the publisher, by accepting the work for publication, acknowledges that the US government retains a non-exclusive, paid-up, irrevocable, world-wide license to publish or reproduce the submitted manuscript version of this work, or allow others to do so, for US government purposes. DOE will provide public access to these results of federally sponsored research in accordance with the DOE Public Access Plan (http://energy.gov/downloads/doe-public-access-plan).

Declaration of interests

The authors report no conflict of interest.

Appendix A. Explicit expressions for the power transfers

The Ho & Craddock (1991) power-transfer analysis has been summarised in § 3. This appendix complements that discussion by providing an equation for the time evolution of the Fourier mode energy (A1) and expressions for the power transfers (A2)–(A7).

A positive power transfer supports mode growth, whereas a negative power transfer corresponds to mode damping. The competition of power transfers determines the Fourier mode energy (E_n in (3.7)) time evolution. This work focuses on the Fourier energy of non-axisymmetric modes ($n \neq 0$), and the equation for their time evolution is obtained by adding the (spectrally decomposed) induction and momentum equations projected into the velocity and magnetic fields, respectively. The resulting equation is

$$\frac{\mathrm{d}E_n}{\mathrm{d}t} = \frac{1}{2}\left(P_{\nabla p_n} + P_{A_n} + P_{\Pi_n} + P_{\eta_n} + P_{PF_n} + P_{L_n}\right). \tag{A1}$$

https://doi.org/10.1017/S0022377822000770 Published online by Cambridge University Press

The power-transfer terms on the right-hand side are defined as follows:

$$\text{pressure gradient: } P_{\nabla p_n} = -2\pi \int_A \boldsymbol{V}_n^* \cdot (\nabla p)_n \, \mathrm{d}A + \text{c.c.}, \tag{A2}$$

$$\text{advective: } P_{A_n} = -2\pi \int_A \rho_0 \boldsymbol{V}_n^* \cdot (\boldsymbol{V} \cdot \nabla \boldsymbol{V})_n \, \mathrm{d}A + \text{c.c.}, \tag{A3}$$

$$\text{viscous dissipation: } P_{\Pi_n} = 2\pi \int_A \boldsymbol{V}_n^* \cdot (\nabla \cdot \Pi)_n \, \mathrm{d}A + \text{c.c.}, \tag{A4}$$

$$\text{resistive dissipation: } P_{\eta_n} = -2\pi \int_A (\eta \boldsymbol{J})_n \cdot \boldsymbol{J}_n^* \, \mathrm{d}A + \text{c.c.}, \tag{A5}$$

$$\text{Poynting flux: } P_{\mathrm{PF}_n} = -2\pi \oint_{\partial A} \cdot \left(\frac{\boldsymbol{E}_n \times \boldsymbol{B}_n^*}{\mu_o} \right) \cdot \boldsymbol{dn} + \text{c.c.}, \tag{A6}$$

$$\text{Lorentz power: } P_{L_n} = 2\pi \int_A \boldsymbol{V}_n^* \cdot (\boldsymbol{J} \times \boldsymbol{B})_n \, \mathrm{d}A + 2\pi \int_A \boldsymbol{J}_n^* \cdot (\boldsymbol{V} \times \boldsymbol{B})_n \, \mathrm{d}A + \text{c.c.} \tag{A7}$$

In these equations, superscript $*$ denotes the complex conjugate, c.c. indicates the complex conjugate of the previous terms and dA is a poloidal cross-sectional differential of area. The physical interpretation of these terms has already been discussed in § 3, but some comments are in order.

Here P_{A_n} is the power transfer associated with the centre of mass advection. Its definition entails the axisymmetric mass density only. During sawtooth cycles analysed here, the non-axisymmetric Fourier mass density components (ρ_k, for $k \neq 0$) are smaller than its axisymmetric part (ρ_0). Equation (A3) is accurate up to $O(\rho_k/\rho_0)$, but this is the same approximation employed in the definition of the leading-order Fourier mode energy, E_n, in (3.7).

We use P_{η_n} to denote the power dissipation due to electrical resistivity. This work includes a Spitzer resistivity in which the electron temperature is fully dependent on position and (A5) takes this into account. The resistive dissipation integrand $(\eta \boldsymbol{J})_n \cdot \boldsymbol{J}_n^*$, differs from $\eta \boldsymbol{J}_n \cdot \boldsymbol{J}_n^* = \eta |\boldsymbol{J}_n|^2$, which is valid for a situation with constant resistivity through the confinement region. Although $\eta |\boldsymbol{J}_n|^2$ is negative definite, $(\eta \boldsymbol{J})_n \cdot \boldsymbol{J}_n^*$ is not. Although individual P_{η_n} contributions may be positive, the sum of P_{η_n} contributions over the complete Fourier spectrum is negative, indicating an overall mode damping effect, as expected from a dissipative power transfer.

The term P_{PF_n} is a conservative term that allows energy flux across the plasma boundary. In this work, it captures the imposed toroidal loop voltage that is responsible for driving ohmic currents that are typically in CTH. Here, only the $n = kN_{\mathrm{fp}}$ fluxes of energy through the plasma boundary are significant. In (A6), ∂A is the boundary of the poloidal cross-section (A) and $\boldsymbol{dn}$ is a vector normal to it.

Appendix B. Posterior sawtooth cycles: an example of a complex fixed-point mechanism during bifurcations

This appendix describes the unexpectedly complicated fixed-point changes that occur early in the second tokamak sawtooth cycle, between the times of figure 3(a) (0.030 ms) and figure 3(b) (0.39 ms).

Figure 9 shows four Poincaré plots, focused on the central plasma region (0.65 m $< R <$ 0.85 m) at times between those of figures 3(a) and 3(b). Figures 3(a) and 9(a) (0.060 ms) both show a single o-point, near the midplane. By the time of figure 9(b) (0.067 ms) an o–x pair has been generated, both located near the midplane. The order in major radius is

https://doi.org/10.1017/S0022377822000770 Published online by Cambridge University Press

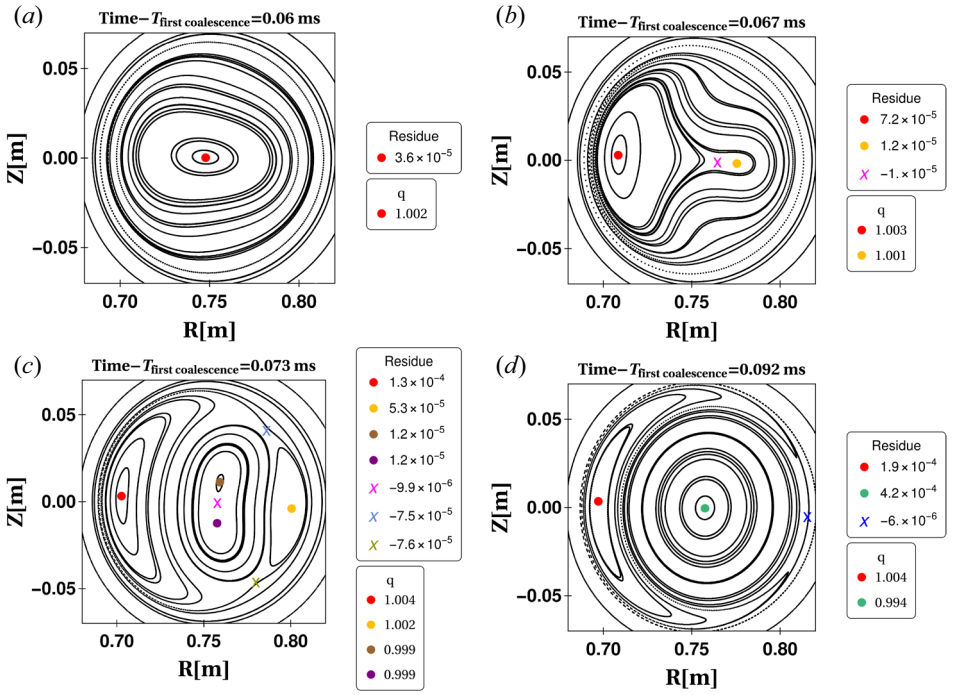

FIGURE 9. Poincaré plots for the tokamak simulation during the $q = 1$ surface emergence of the second sawtooth cycle.

o–*x*–*o*. Just 6 μs later, in figure 9(*c*) (0.073 ms) two more *o*–*x* pairs have been generated, one pair above and one pair below the midplane. By the time of figure 9(*d*) (0.092 ms) the two off-midplane *o*-points have merged with the on-midplane *x*-point to form an on-midplane *o*-point, at approximately $R = 0.071$ m. In addition, the two off-midplane *x*-points have merged with the outer on-midplane *o*-point to form an on-midplane *x*-point, at approximately $R = 0.082$ m. The configuration of figure 9(*d*) shows three near-midplane fixed points with major radius order *o*–*o*–*x*, the same as in figure 3(*b*).

It is important to note that all of the *o*-points in figure 9 have limiting q values very close to 1. Thus, only a very small change in the magnetic field is required to cause the fixed-point topology changes that are shown in figure 9.

REFERENCES

ALEYNIKOVA, K., HUDSON, S.R., HELANDER, P., KUMAR, A., GEIGER, J., HIRSCH, M., LOIZU, J., NÜHRENBERG, C., RAHBARNIA, K., QU, Z., *et al.* 2021 Model for current drive induced crash cycles in W7-X. *Nucl. Fusion* **61** (12), 126040.

ARA, G., BASU, B., COPPI, B., LAVAL, G., ROSENBLUTH, M.N. & WADDELL, B.V. 1978 Magnetic reconnection and $m = 1$ oscillations in current carrying plasmas. *Ann. Phys.* **112**, 443–476.

CARRERAS, B.A., LYNCH, V.E., ZUSHI, H., ICHIGUCHI, K. & WAKATANI, M. 1998 Internal disruptions in Heliotron E*. *Phys. Plasmas* **5** (10), 3700–3707.

CARY, J.R. & HANSON, J.D. 1986 Stochasticity reduction. *Phys. Fluids* **29** (8), 2464–2473.

CHOI, S., CRAIG, D., EBRAHIMI, F. & PRAGER, S.C. 2006 Cause of sudden magnetic reconnection in a laboratory plasma. *Phys. Rev. Lett.* **96**, 145004.

COPPI, B., GALVAO, R., PELLAT, R., ROSENBLUTH, M. & RUTHERFORD, P. 1976 Resistive internal kink modes. *Sov. J. Plasma Phys.* **2**, 533–535.

https://doi.org/10.1017/S0022377822000770 Published online by Cambridge University Press

FUTCH, A.M., CRAIG, D., HESSE, R. & JACOBSON, C.M. 2018 Role of resistivity and viscosity in the excitation of stable $m = 0$ modes during the RFP sawtooth crash. *Phys. Plasmas* **25** (11), 112506.

VON GOELER, S., STODIEK, W. & SAUTHOFF, N. 1974 Studies of internal disruptions and $m = 1$ oscillations in tokamak discharges with soft-X-Ray techniques. *Phys. Rev. Lett.* **33**, 1201–1203.

GREENE, J.M. 1968 Two-dimensional measure-preserving mappings. *J. Math. Phys.* **9** (5), 760–768.

GREENE, J.M. 1979 A method for determining a stochastic transition. *J. Math. Phys.* **20** (6), 1183–1201.

HANSON, J.D. & CARY, J.R. 1984 Elimination of stochasticity in stellarators. *Phys. Fluids* **27** (4), 767–769.

HARTWELL, G.J., KNOWLTON, S.F., HANSON, J.D., ENNIS, D.A. & MAURER, D.A. 2017 Design, construction, and operation of the compact toroidal hybrid. *Fusion Sci. Technol.* **72** (1), 76–90.

HERFINDAL, J.L., MAURER, D.A., HARTWELL, G.J., ENNIS, D.A., HANSON, J.D., KNOWLTON, S.F., MA, X., PANDYA, M.D., ROBERDS, N.A. & TRAVERSO, P.J. 2019 Sawtooth oscillation behavior with varying amounts of applied stellarator rotational transform. *Phys. Plasmas* **26** (3), 032502.

HOWELL, E.C., KING, J.R., KRUGER, S.E., CALLEN, J.D., LA HAYE, R.J. & WILCOX, R.S. 2022 Growing neoclassical tearing modes seeded via transient-induced-multimode interactions. *Phys. Plasmas* **29** (2), 022507.

HO, Y.L. & CRADDOCK, G.G. 1991 Nonlinear dynamics of field maintenance and quasiperiodic relaxation in reversed-field pinches. *Phys. Fluids* B **3** (3), 721–734.

KADOMTSEV, B.B. 1975 Disruptive instability in tokamaks. *Sov. J. Plasma Phys.* **1** (2), 389–391.

LA HAYE, R.J. 2006 Neoclassical tearing modes and their control. *Phys. Plasmas* **13** (5), 055501.

REYNOLDS, J.M., SOVINEC, C.R. & PRAGER, S.C. 2008 Nonlinear magnetohydrodynamics of pulsed parallel current drive in reversed-field pinches. *Phys. Plasmas* **15** (6), 062512.

ROBERDS, N.A., GUAZZOTTO, L., HANSON, J.D., HERFINDAL, J.L., HOWELL, E.C., MAURER, D.A. & SOVINEC, C.R. 2016 Simulations of sawtoothing in a current carrying stellarator. *Phys. Plasmas* **23** (9), 092513.

SAUTER, O., LA HAYE, R.J., CHANG, Z., GATES, D.A., KAMADA, Y., ZOHM, H., BONDESON, A., BOUCHER, D., CALLEN, J.D., CHU, M.S., *et al.* 1997 Beta limits in long-pulse tokamak discharges. *Phys. Plasmas* **4** (5), 1654–1664.

SMIET, C.B., KRAMER, G.J. & HUDSON, S.R. 2019 Mapping the sawtooth. *Plasma Phys. Control. Fusion* **62** (2), 025007.

SOVINEC, C.R. 1995 Magnetohydrodynamic simulations of noninductive helicity injection in the reversed-field pinch and tokamak. PhD thesis, University of Wisconsin, Madison, WI.

SOVINEC, C.R., GLASSER, A.H., GIANAKON, T.A., BARNES, D.C., NEBEL, R.A., KRUGER, S.E., PLIMPTON, S.J., TARDITI, A. Chu, M.S. & THE NIMROD TEAM 2004 Nonlinear magnetohydrodynamics with high-order finite elements. *J. Comput. Phys.* **195**, 355.

SPONG, D.A. 2015 3D toroidal physics: testing the boundaries of symmetry breaking. *Phys. Plasmas* **22** (5), 055602.

TAKAGI, S., TOI, K., TAKECHI, M., MURAKAMI, S., TANAKA, K., NISHIMURA, S., ISOBE, M., MATSUOKA, K., MINAMI, T., OKAMURA, S., *et al.* 2004 Characteristics of sawtooth oscillations observed in the compact helical system. *Phys. Plasmas* **11** (4), 1537–1544.

VARELA, J., WATANABE, K.Y. & OHDACHI, S. 2012 The internal disruption as hard magnetohydrodynamic limit of 1/2 sawtooth like activity in large helical device. *Phys. Plasmas* **19** (8), 082512.

ZANINI, M., LAQUA, H.P., THOMSEN, H., STANGE, T., BRANDT, C., BRAUNE, H., BRUNNER, K.J., FUCHERT, G., HIRSCH, M., KNAUER, J., *et al.* 2020 ECCD-induced sawtooth crashes at W7-X. *Nucl. Fusion* **60** (10), 106021.